JACS
JOURNAL OF THE AMERICAN CHEMICAL SOCIETY
Article
Cite This: J. Am. Chem. Soc. 2019, 141, 20155−20165
pubs.acs.org/JACS

Crystallization of Mordenite Platelets using Cooperative Organic Structure-Directing Agents

Manjesh Kumar,[†] Zachariah J. Berkson,[‡] R. John Clark,[†] Yufeng Shen,[†] Nathan A. Prisco,[‡] Qi Zheng,[§] Zhiyuan Zeng,[§,∥] Haimei Zheng,[§,∥] Lynne B. McCusker,[‡,⊥] Jeremy C. Palmer,[†] Bradley F. Chmelka,[*,‡] and Jeffrey D. Rimer[*,†]

[†]Department of Chemical and Biomolecular Engineering, University of Houston, 4726 Calhoun Road, Houston, Texas 77204, United States
[‡]Department of Chemical Engineering, University of California, Santa Barbara, Santa Barbara, California 93106, United States
[§]Materials Sciences Division, Lawrence Berkeley National Laboratory, 1 Cyclotron Road, Berkeley, California 94720, United States
[∥]Department of Materials Science and Engineering, University of California, Berkeley, California 94720, United States
[⊥]Department of Materials, ETH Zurich, Vladimir-Prelog-Weg 5, CH-8093 Zurich, Switzerland

Supporting Information

ABSTRACT: Organic structure-directing agents (OSDAs) are exploited in the crystallization of microporous materials to tailor the physicochemical properties of the resulting zeolite for applications ranging from separations to catalysis. The rational design of these OSDAs often entails the identification of molecules with a geometry that is commensurate with the channels and cages of the target zeolite structure. Syntheses tend to employ only a single OSDA, but there are a few examples where two or more organics operate synergistically to yield a desired product. Using a combination of state-of-the-art characterization techniques and molecular modeling, we show that the coupling of *N*,*N*,*N*-trimethyl-1,1-adamantammonium and 1,2-hexanediol, each yielding distinct zeolites when used alone, results in the cooperative direction of a third structure, HOU-4, with the mordenite framework type (**MOR**). Rietveld refinement using synchrotron X-ray diffraction data reveals the spatial arrangement of the organics in the HOU-4 crystals, with amines located in the large channels and alcohols oriented in the side pockets lining the one-dimensional pores. These results are in excellent agreement with molecular dynamics calculations, which predict similar spatial distributions of organics with an energetically favorable packing density that agrees with experimental measurements of OSDA loading, as well as with solid-state two-dimensional $^{27}Al\{^{29}Si\}$, $^{27}Al\{^{1}H\}$, and $^{13}C\{^{1}H\}$ NMR correlation spectra, which establish the proximities and interactions of occluded OSDAs. A combination of high-resolution transmission electron microscopy and atomic force microscopy is used to quantify the size of the HOU-4 crystals, which exhibit a platelike morphology, and to index the crystal facets. Our findings reveal that the combined OSDAs work in tandem to produce ultrathin, nonfaulted HOU-4 crystals that exhibit improved catalytic activity for cumene cracking in comparison to mordenite crystals prepared via conventional syntheses. This novel demonstration of cooperativity highlights the potential possibilities for expanding the use of dual structure-directing agents in zeolite synthesis.

INTRODUCTION

The demand for more efficient zeolite catalysts creates a need to develop new synthesis approaches capable of tailoring crystal properties for optimal performance. Among the many physicochemical properties of zeolites, crystal size plays a significant role in mediating internal mass transport,[1,2] wherein diffusion path lengths of less than 100 nm can markedly improve catalyst lifetime and alter product selectivity.[3] Various approaches have been explored to tune the anisotropic growth of zeolite crystals precisely, including the modification of synthesis conditions, the introduction of growth modifiers,[4] the design of new organic structure-directing agents (OSDAs),[5−9] and the use of crystalline seeds.[10] Achieving materials with well-controlled properties is often challenging, because the mechanisms of zeolite crystallization[11−14] are complex and poorly understood. Here, we combine state of the art X-ray powder diffraction (XPD) and solid-state NMR characterization techniques with computer modeling to examine the role of OSDAs in the formation of the mordenite framework type (**MOR**),[15] which is difficult to prepare with submicrometer dimensions.[16]

Mordenite is a large-pore zeolite (pore diameter ca. 0.7 nm) with unidirectional channels aligned along the *c* axis that is used as a commercial catalyst in reactions such as dehydration of alcohols to olefins,[17] oxidation of methane to methanol,[18]

Received: September 7, 2019
Published: November 21, 2019

DOI: 10.1021/jacs.9b09697
J. Am. Chem. Soc. 2019, 141, 20155−20165

(hydro)isomerization,[19] cracking,[20] alkylation,[21] and carbonylation.[22] Prior studies have attributed the catalytic activity of mordenite to the intersection of 12-ring channels with 8-ring side pockets (Figure S1) that facilitate shape-selective reactions; however, mordenite is highly susceptible to deactivation owing to mass transport limitations imposed by its one-dimensional pores and large channels that facilitate the formation of polyaromatics (i.e., coke precursors). The reported syntheses of mordenite typically yield large crystallites with sizes that range from 5 to 20 μm and with stacking faults that alter the placement of 8-ring pockets within the channels.[23,24] Postsynthesis modification to introduce mesoporosity is one way of mitigating internal diffusion limitations.[25] Alternatively, the synthesis of crystallites with submicrometer dimensions of the [001] facet can extend the catalyst lifetime. Suib and co-workers have reported sizes as small as 40−60 nm using complicated synthesis protocols that include the use of crystalline seeds,[26] alcohol additives, and/or microwave heating.[27] Mordenite nanorods (ca. 10 × 100 nm) have been synthesized using seeds or cationic gemini surfactants by Xiao[28] and Ryoo[29] and their co-workers, respectively. These syntheses have resulted in nanometer-sized domains within larger aggregates, which similarly involve limitations in internal mass transport.

A combination of inorganic and organic structure-directing agents are often used in zeolite syntheses to regulate the kinetics of crystallization.[30] The synthesis of most zeolites requires the use of OSDA molecules with sizes and shapes that are commensurate with the cages/channels of the target zeolite, thereby facilitating the generation of the desired porous structure.[7] OSDAs are occluded within the framework and are typically removed by postsynthesis calcination. It is common practice to use a single OSDA. In select cases, OSDAs can form clusters (e.g., dimers or aggregates) to stabilize the framework.[31,32] Few syntheses employ two or more different OSDAs. Examples often involve scenarios where only one organic functions as the OSDA and the other alters properties such as crystal size or habit but is a bystander for structure direction.[33] Combinations of OSDAs have also been used to prevent polymorphism in order to improve product purity.[34] Wright and co-workers have demonstrated for zeotypes, such as STA-20, that two organics may be necessary to achieve a desired crystalline phase.[35] In such cases, the OSDAs act cooperatively to produce a product that could not be achieved with either one alone.

Herein, we demonstrate how two OSDAs (one bearing a quaternary amine group and the other an alcohol) cooperatively direct the formation of mordenite crystals with an ultrathin platelet morphology unlike that obtained with conventional methods. The synthesis condition selected for this study produces two different framework types (**MFI**- or **CHA**-type zeolites) when each OSDA is used separately; however, the combination of organics yields mordenite. In order to elucidate the spatial distribution of organics within the channels and side pockets of the mordenite crystals, we used a combination of high-resolution electron microscopy, spectroscopy, and diffraction techniques coupled with molecular modeling to show how the distinct combination of OSDAs works synergistically to direct the mordenite framework structure. A parametric evaluation of synthesis conditions reveals that the judicious selection of OSDAs and growth media and conditions is critical to the formation of mordenite.

RESULTS AND DISCUSSION

Our findings have shown that two OSDAs, *N*,*N*,*N*-trimethyl-1,1-adamantammonium (TMAda$^+$) and 1,2-hexanediol ($D6_{1,2}$), work cooperatively to yield a **MOR**-type zeolite, referred to hereafter as HOU-4. TMAda$^+$ is a well-documented OSDA for commercial SSZ-13 (**CHA**) (Figure 1A). The same

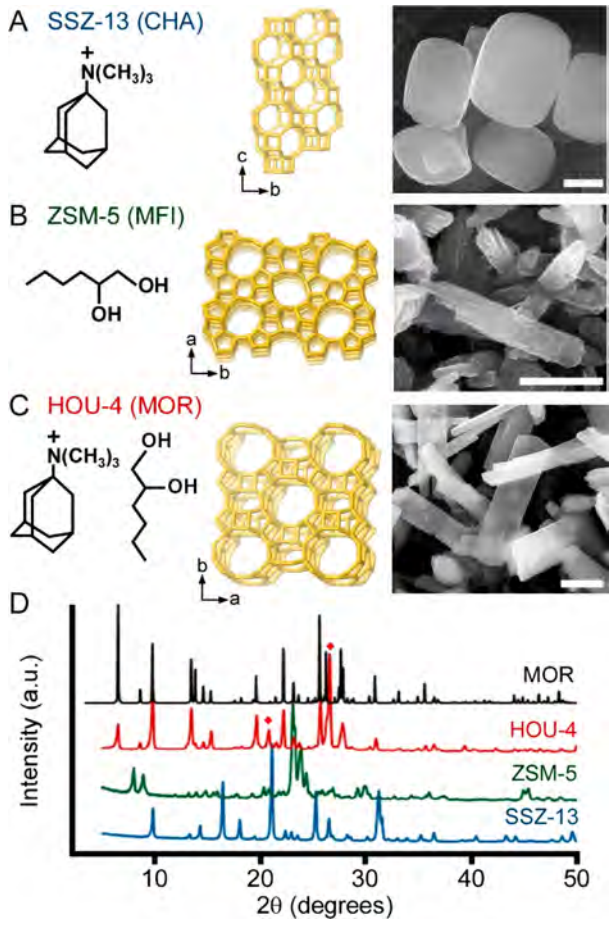

Figure 1. OSDA(s), corresponding zeolite structure, and representative scanning electron micrograph for (A) SSZ-13 (**CHA**) prepared with TMAda$^+$, (B) ZSM-5 (**MFI**) prepared with $D6_{1,2}$ or Na^+ ions, and (C) HOU-4 (**MOR**) prepared with TMAda$^+$ and $D6_{1,2}$. Scale bars equal 1 μm. (D) X-ray powder diffraction patterns of the solid precipitates obtained after 6 days of hydrothermal treatment at 180 °C (Table S1) confirming the formation of SSZ-13 (blue), ZSM-5 (green), and HOU-4 (red). The structure of HOU-4 was confirmed using a reference pattern for mordenite (black). Reflections corresponding to a quartz impurity in the HOU-4 sample (Figure S6) are labeled with diamonds. The presence of quartz is attributed to excess silica in the reaction mixture. Parametric studies reduced the quantity of quartz but were unable to eliminate the impurity entirely (see the Supporting Information for more details).

synthesis using only $D6_{1,2}$ results in ZSM-5 (**MFI**) (Figure 1B), whereas an organic-free synthesis with Na^+ as an inorganic structure-directing agent also yields ZSM-5 (Figures S2 and S3). Interestingly, the combination of $D6_{1,2}$ and TMAda$^+$ in solutions containing Na^+ produces HOU-4 (Figure 1C and Figure S4). Thus, we observe that individual OSDAs and their binary combination generate three different zeolites (Figure 1D): ZSM-5 is a three-dimensional medium-pore zeolite, SSZ-13 is a three-dimensional small-pore zeolite, and mordenite is a one-dimensional large-pore zeolite. The

DOI: 10.1021/jacs.9b09697
J. Am. Chem. Soc. 2019, 141, 20155−20165

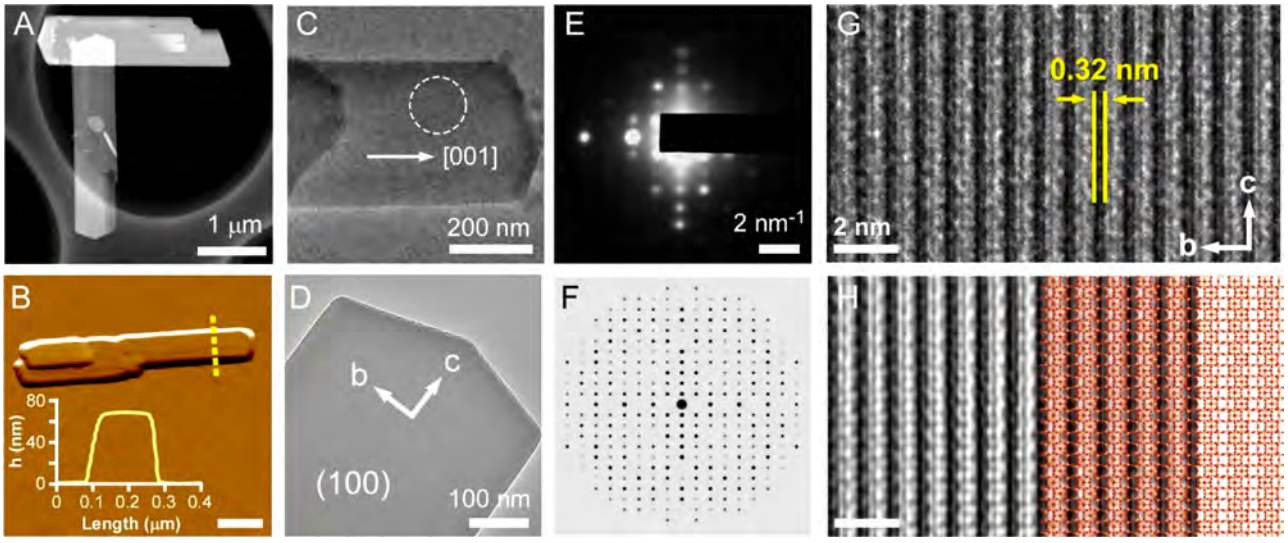

Figure 2. Indexing the habit of HOU-4 crystals. (A) High-angle annular dark-field (HAADF) STEM image of representative HOU-4 crystals taken at low magnification. (B) AFM amplitude mode image of a crystal in air. Inset: height profile measured along the dashed line. The scale bar equals 500 nm. (C) TEM image of a HOU-4 crystal with the [001] growth direction highlighted (arrow). (D) Indexed HOU-4 crystal with a (100) basal surface. (E) Selected area electron diffraction (SAED) pattern of the region in (C) marked by the dashed white circle. The zone axis is [100]. (F) Simulated SAED pattern from [100] based on the mordenite crystal structure (see Figure S12 for patterns of the [010] and [001] zone axes). (G) High-resolution TEM image of a HOU-4 crystal along the [100] zone axis. The black strips could be regarded as pore channels. (H) HRTEM image in (G) after application of a Fourier filter, overlaid with the crystal structure model of mordenite along the [100] direction. Atoms are color-coded as red (oxygen) and yellow (silicon or aluminum).

composite building units (CBUs)[15] of these three structures are different, with the exception of *mor* being shared by both **MFI** and **MOR** framework types (Figure S5). The three zeolites have similar elemental compositions (Table S2) but differ with respect to the crystal habit and quantity of occluded OSDA (Figure S7 and Table S3).

SSZ-13 crystals have a spheroidal morphology with sizes of 1−2 μm and 10 wt % organic (ca. 1.3 $TMAda^+$ per unit cell). ZSM-5 crystals exhibit an indistinct morphology with submicrometer dimensions and contain 5 wt % organic (ca. 2.7 $D6_{1,2}$ per unit cell). HOU-4 crystallizes as thin platelike particles that retain ca. 2 $D6_{1,2}$ and 2 $TMAda^+$ molecules per unit cell, as determined from synchrotron XPD data (Figure S8). All of the $D6_{1,2}$ molecules are removed by postsynthetic washing with water (Figures S9 and S10), which establishes that $D6_{1,2}$ molecules are able to diffuse out of the mordenite nanochannels without appreciable restrictions. The mobility of $D6_{1,2}$ within the large pore channels of mordenite was corroborated by molecular dynamics (MD) simulations (Movie S1). Facile extraction of the diol molecules from zeolite frameworks without the need for postsynthesis calcination is uncommon; therefore, the synthesis of HOU-4 offers a unique route to recover and potentially recycle the OSDAs.

Comparison of transmission electron micrographs from multiple batches (Figure 2A,C,D) show that the width of the HOU-4 crystallites in the [010] direction can reach 1 μm with an average length to width (or [001]/[010]) aspect ratio of 4.0 ± 0.7. Atomic force microscopy (AFM) topographical images of HOU-4 crystals (Figure 2B) reveal an ultrathin habit wherein the analysis of numerous crystals shows a distribution of thicknesses in the [100] direction of around 80 nm (see Figure S11). Selected-area electron diffraction patterns (Figure 2E) were compared against simulated patterns for mordenite along the three principal crystallographic directions (Figure 2F and Figure S12). These comparisons confirm that the basal surface of HOU-4 is the (100) face. High-resolution TEM (HRTEM, Figure 2G) and the corresponding Fourier filtered image (Figure 2H) show that the 1D channels are oriented parallel to the longest dimension of the HOU-4 crystals. The indexing was further corroborated by overlaying the framework structure of mordenite along the [100] direction on the filtered HRTEM image (Figure 2H), revealing an excellent match. Prior crystallographic analyses of synthetic mordenite commonly assign the six-edged surface as the (001) face.[24,36,37] Indeed, this general morphology is characteristic of most mordenite crystals prepared in the absence of organics (for example, see Figure 6). Assuming that the indexing of the facets of conventional mordenite crystals is correct, it appears that the cooperativity of OSDAs dramatically alters the HOU-4 crystal habit in ways that are neither predictable nor fully understood.

In order to ascertain the spatial arrangement of OSDAs within the zeolite channels, we analyzed an unwashed HOU-4 sample using synchrotron XPD data (Figure 3A) and confirmed that $TMAda^+$ resides within the 12-ring channels (Figure 3B,D), Na^+ in the oval 8-ring channels, and $D6_{1,2}$ in the 8-ring side pockets (Figure 3C). Rietveld refinement of the framework structure with occluded structure-directing agents indicates that there are two Na^+, two $TMAda^+$, two $D6_{1,2}$ and two water molecules per unit cell. No evidence of crystallite shape anisotropy or stacking faults was apparent in the peak-shape profiles or in the structure refinement. HOU-4 appears to be free of the stacking disorder along the *c* direction that is present in many mordenite syntheses. Quantitative solid-state one-dimensional (1D) single-pulse ^{13}C and ^{1}H magic-angle-spinning (MAS) NMR analyses (Figure S14) yield a much larger quantity of $D6_{1,2}$ (~10 $D6_{1,2}/TMAda^+$). This suggests that unwashed samples probably retain significant quantities of diol molecules on the particle surfaces, and this is in agreement

DOI: 10.1021/jacs.9b09697
J. Am. Chem. Soc. 2019, 141, 20155−20165

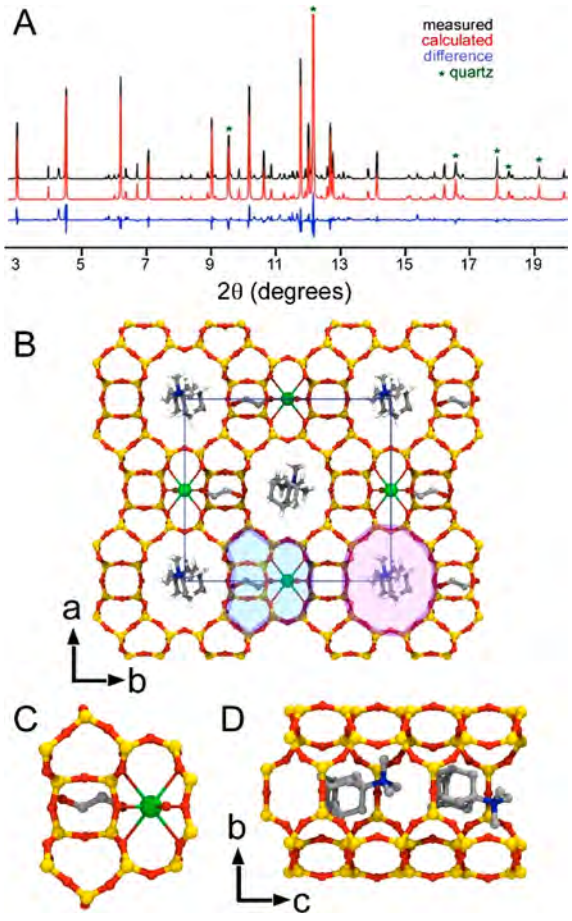

Figure 3. Rietveld refinement of HOU-4 using synchrotron powder diffraction data. (A) Measured (black), calculated (red), and difference profiles (blue) (Table S4). Reflections from a quartz impurity are marked with a green asterisk. (B–D) Arrangement of the nonframework species within the channels of the **MOR** framework compatible with the refined structure of HOU-4 (see also Figure S13): (B) view down the *c* axis; (C) close-up of the 8-ring side pocket (highlighted in blue in (B)) showing the octahedral coordination of a Na^+ ion to four framework oxygen atoms, one water molecule and one $D6_{1,2}$ molecule; (D) orthogonal view of the 12-ring channel (highlighted in pink in (B)) showing the arrangement of $TMAda^+$ ions along the channel. Atoms are color-coded as gray (carbon), red (oxygen), blue (nitrogen), white (hydrogen), green (sodium), and yellow (T sites occupied by silicon or aluminum).

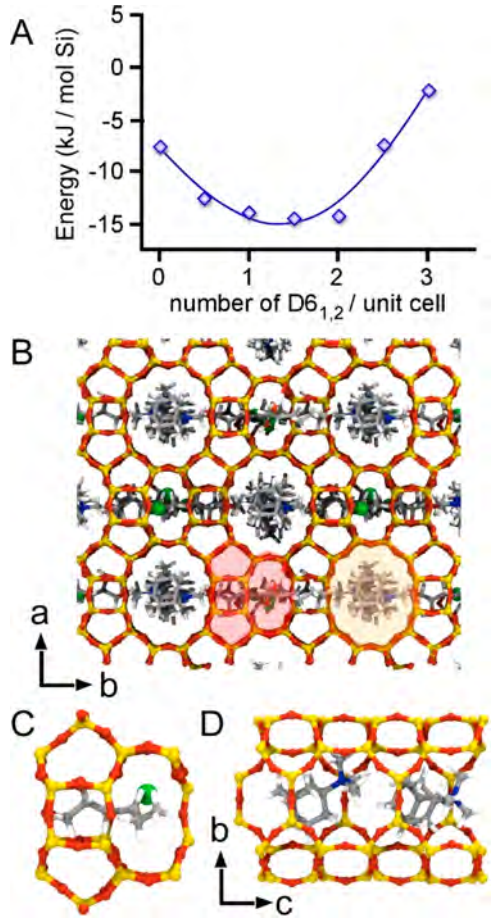

Figure 4. Molecular simulations of organic occlusion in HOU-4 channels. (A) MD calculation of the stabilization energy for organics occluded in mordenite as a function of $D6_{1,2}$ loading using a fixed 1.5 $TMAda^+$ per unit cell. The solid line is a guide for the eye. (B–D) MD simulation of OSDA molecules aligned within the 12-ring channel: (B) view along the *c* direction; (C) $D6_{1,2}$ aligned within the 8-ring pocket; (D) $TMAda^+$ molecules arranged in the 12-ring channel. Images (C) and (D) contain two Na^+, two $TMAda^+$, and two $D6_{1,2}$ per unit cell. Atoms are color-coded as gray (carbon), red (oxygen), blue (nitrogen), white (hydrogen), green (sodium), and yellow (T sites occupied by silicon or aluminum).

with thermogravimetric analysis of unwashed HOU-4 showing 37 wt% mass loss, consistent with the desorption of surface-adsorbed diol molecules (Figure S7C).

To further understand the role of occluded organics in HOU-4, we performed MD simulations of both OSDAs and Na^+ ions in mordenite. Models placing an increasing amount of alcohol within a single mordenite unit cell at fixed $TMAda^+$ loading (Figure 4A) show that alcohols stabilize the structure, leading to a minimum in the energy profile at around 1.5–2.0 $D6_{1,2}$ molecules per unit cell. This indicates that the alcohol is not merely acting as a space filler[38] but has a significant effect on the energetics of crystallization. As the quantity of $TMAda^+$ per unit cell is increased, less alcohol is required to minimize the energy (Figure S15). In agreement with XPD data revealing the presence of $TMAda^+$ within the large pores of HOU-4, MD simulations show that $TMAda^+$ is energetically favored to be within the 12-ring channels (Figure 4B,D) with the amine groups oriented in close proximity to the 8-ring pockets. At high $TMAda^+$ loading (two per unit cell), $D6_{1,2}$ molecules are oriented within the 8-ring pockets (Figure 4C), consistent with the XPD refinement. At lower $TMAda^+$ loadings, $D6_{1,2}$ molecules are also observed to reside within the 12-ring channels between adjacent $TMAda^+$ molecules (Figure S16). Hence, both experiment and simulation suggest that the two OSDAs direct the formation of mordenite in a synergistic fashion by stabilizing different features of the framework: $TMAda^+$ directs growth of the 12-ring channels, whereas $D6_{1,2}$ predominantly functions by stabilizing the 8-ring pockets.

The site-specific interactions of different framework ^{27}Al species with OSDA molecules are established by solid-state two-dimensional (2D) heteronuclear correlation (HETCOR) NMR spectra of HOU-4 (Figure 5). The 2D NMR correlation spectra exploit internuclear dipole–dipole (through-space) or *J* (through-covalent-bond) couplings and are plotted as 2D contour plots, where correlated signal intensities manifest the mutual proximities or covalent connectivities of the corre-

DOI: 10.1021/jacs.9b09697
J. Am. Chem. Soc. 2019, 141, 20155–20165

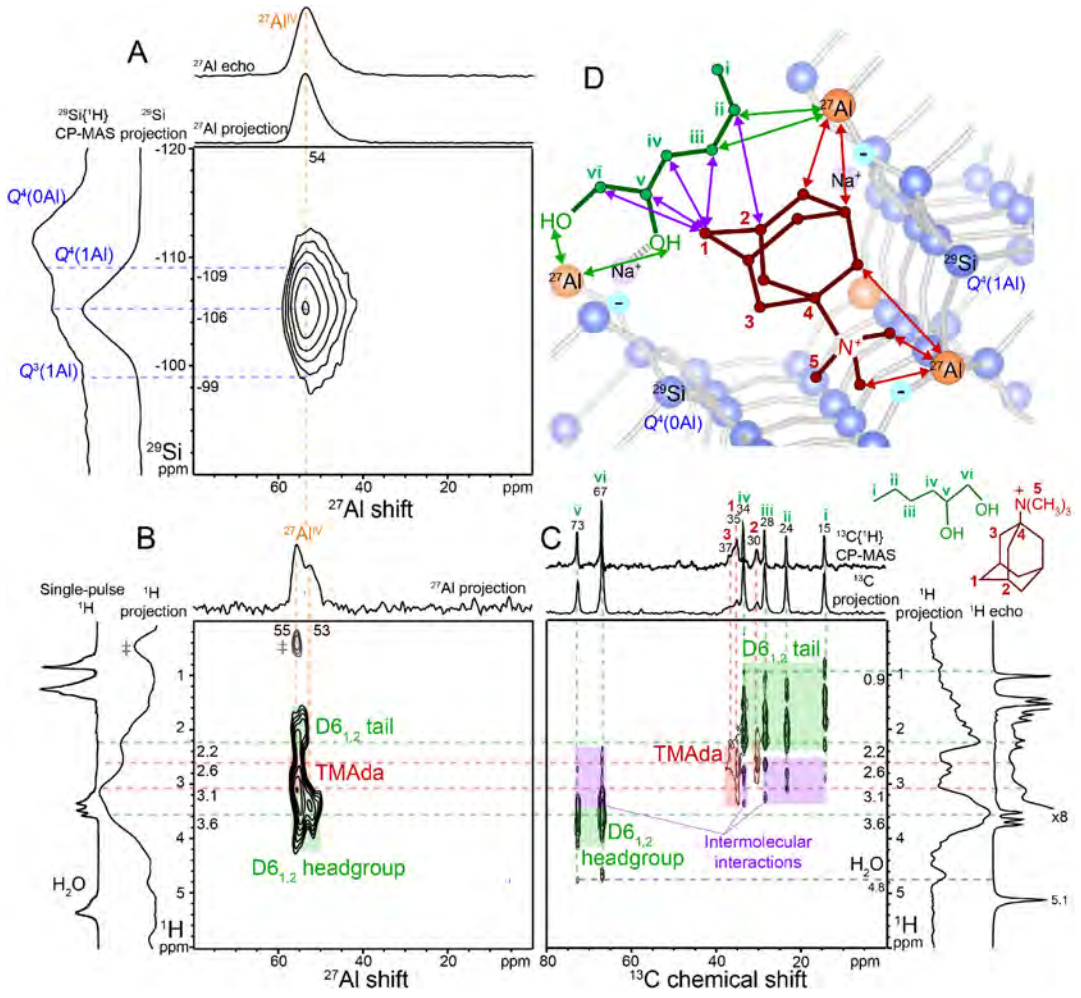

Figure 5. (A) Solid-state 2D ^{27}Al{^{29}Si} *J*-mediated NMR correlation spectrum acquired at 95 K, 9.4 T, and 10 kHz MAS. (B) Solid-state 2D ^{27}Al{^{1}H} HETCOR spectrum acquired at 263 K, 18.8 T, and 12.5 kHz MAS with a ^{27}Al{^{1}H} contact time of 0.5 ms. The ‡ symbol indicates a center-frequency artifact (for more details refer to the Supporting Information). (C) Solid-state 2D ^{13}C{^{1}H} HETCOR spectrum acquired at 263 K, 11.7 T, and 2.5 kHz MAS with a ^{13}C{^{1}H} contact time of 5 ms. All of the ^{13}C signals are assigned to ^{13}C moieties on the TMAda$^+$ and D6$_{1,2}$ molecules, as indicated in the inset molecular structures. 1D ^{27}Al, ^{13}C{^{1}H}, or ^{1}H MAS NMR spectra acquired under the same conditions are shown along the corresponding ^{27}Al, ^{13}C, or ^{1}H axes for comparison with the 1D projections of the 2D spectra. (D) Schematic diagram of framework-OSDA and intermolecular interactions established by 2D NMR analyses. Green and red arrows indicate framework ^{27}Al interactions with D6$_{1,2}$ and TMAda$^+$ molecules, respectively; purple arrows indicate intermolecular interactions of commingled OSDA molecules.

sponding ^{1}H, ^{13}C, ^{27}Al, or ^{29}Si species.[39,40] For example, covalent ^{27}Al−O−^{29}Si bonds within the HOU-4 frameworks are unambiguously established by the 2D ^{27}Al{^{29}Si} *J*-mediated NMR correlation spectrum (Figure 5A), which shows a distribution of correlated signal intensity at 54 ppm in the ^{27}Al dimension and −109 to −99 ppm in the ^{29}Si dimension arising from framework aluminum atoms bonded to fully or partially cross-linked ^{29}Si atoms. Previously, such 2D ^{27}Al{^{29}Si} through-bond-mediated correlation spectra of aluminosilicate zeolites have been limited due in part to the low natural isotopic abundance of ^{29}Si (4.7%) and weak ^{27}Al−O−^{29}Si *J* couplings (<20 Hz) but are enabled here by the improved sensitivity of low-temperature measurement conditions. The ^{27}Al signals exhibit Czjzek lineshapes[41] that reflect a distribution of ^{27}Al heteroatom environments within the mordenite framework and among the four distinct tetrahedral (T) sites, corroborated by complementary ^{27}Al triple-quantum MAS NMR analyses (Figure S17). The relatively small percentage of partially cross-linked ^{29}Si species (ca. 2%, Figure S18) are probably associated with defect sites at the exterior of the particle surfaces. The Si/Al ratio of HOU-4 estimated by quantitative ^{29}Si MAS NMR is ca. 10 (Figure S18), which is consistent with values of ca. 10 and 13 measured by energy-dispersive X-ray spectroscopy (Table S2) and estimated from synchrotron XPD refinement, respectively.

Different types of framework aluminum sites in as-made HOU-4 are distinguished on the basis of their site-specific interactions with different OSDA molecules, which are established by the 2D ^{27}Al{^{1}H} (Figure 5B) and ^{13}C{^{1}H} HETCOR (Figure 5C) NMR spectra. The HETCOR spectra yield correlated ^{13}C−^{1}H or ^{27}Al−^{1}H signal intensities from ^{13}C−^{1}H or ^{27}Al−^{1}H nuclear spin pairs that are dipole−dipole-coupled through space over subnanometer distances. The different ^{1}H and ^{13}C signals are assigned to ^{1}H and ^{13}C moieties on D6$_{1,2}$ (green shaded regions) or TMAda$^+$ (red shaded regions) molecules by analyses of complementary solid-state 1D and 2D ^{13}C{^{1}H} NMR spectra (Figures S10 and S14) and solution-state 1D ^{13}C NMR spectra of the zeolite synthesis effluent (Figure S19). The 2D ^{27}Al{^{1}H} HETCOR spectrum (Figure 5B) resolves two ^{27}Al signals: one at 55 ppm,

DOI: 10.1021/jacs.9b09697
J. Am. Chem. Soc. 2019, 141, 20155−20165

which is correlated to ^{1}H signals at 2.2 to 3.6 ppm from TMAda^{+} and D6$_{1,2}$ ^{1}H moieties, and one at 53 ppm, which is correlated only to the ^{1}H signal at 3.6 ppm from D6$_{1,2}$ alcohol headgroups coordinated to Na^{+} cations.[42] These correlated signals evidence two different types of framework ^{27}Al species with either TMAda^{+} or Na^{+} cations charge-balancing the associated framework negative charges. As the TMAda^{+} molecules are sterically hindered from entering the 8-ring mordenite channels, the framework ^{27}Al species proximate to TMAda^{+} cations are expected to be within the 12-ring channels. Those framework ^{27}Al species associated with charge-balancing Na^{+} cations are likely located within the 8-ring pockets where the Na^{+} species are positioned, as determined by the synchrotron XPD analysis (Figure 3) and as corroborated by 2D ^{23}Na{^{1}H} HETCOR analyses (Figure S20).

Furthermore, the different OSDA molecules are in close mutual proximities within the mordenite channels, as established by the 2D ^{13}C{^{1}H} HETCOR spectrum of HOU-4 (Figure 5C). This spectrum shows correlated signals at 2.2−3.1 ppm in the ^{1}H dimension and at ^{13}C shifts of 15, 24, 28, 34, 67, and 73 ppm (purple shaded regions) that arise from intermolecular interactions of ^{1}H environments in TMAda^{+} molecules and the different ^{13}C environments in proximate (<1 nm) D6$_{1,2}$ molecules. On the basis of complementary 2D ^{29}Si{^{1}H} HETCOR spectra (Figure S21) and the synchrotron XPD analyses, we conclude that the different OSDA molecules are intimately commingled within the zeolite pores and act cooperatively (as schematically shown in Figure 5D) during the hydrothermal syntheses of HOU-4 to direct the formation of the mordenite framework and the distribution of Al heteroatoms within both the linear 12-ring channels and the 8-ring pockets.

Parametric studies of HOU-4 synthesis reveal a sensitivity to growth mixture composition (Figures S22−S25). The composition selected for this study (solution C1) falls within the range typically reported for organic-free ZSM-5.[43] Attempts to prepare HOU-4 in growth mixtures more commonly reported for mordenite (i.e., solution C5 with both OSDAs) at higher aluminum content resulted in much larger crystals. Mordenite is typically synthesized using Na^{+} ions as the sole structure-directing agent, which leads to crystals with a large variance in size and shape (Figure 6). Introduction of D6$_{1,2}$ and/or TMAda^{+} to conventional synthesis mixtures does not markedly reduce the crystal size. Indeed, the growth mixture that generates HOU-4 is adopted from a SSZ-13 synthesis,[44] where we have reported D6$_{1,2}$ to be an effective modifier of SSZ-13 crystallization at low concentration (i.e., molar ratios less than 1.0 D6$_{1,2}$ to 1.0 SiO_2). Under such conditions, the diol reduces the size of SSZ-13 crystals by 1 order of magnitude; however, increased diol content (i.e., molar ratios in excess of 1.6 D6$_{1,2}$ to 1.0 SiO_2) shifts its role from that of crystal growth modifier to an OSDA that operates synergistically with TMAda^{+} to direct the formation of ultrathin mordenite crystals. This reveals that HOU-4 requires a threshold amount of diol and growth mixtures with much higher silicon content than are typically required for conventional mordenite synthesis.

The formation of HOU-4 and its purity are sensitive to the carbon length of the diol. For example, combinations of TMAda^{+} with either 1,2-pentanediol (Figure 7A) or 1,2-butanediol (Figure S25) lead to a SSZ-13 impurity, whereas 1,2-propanediol (Figure 7B) results in pure SSZ-13. Diols with

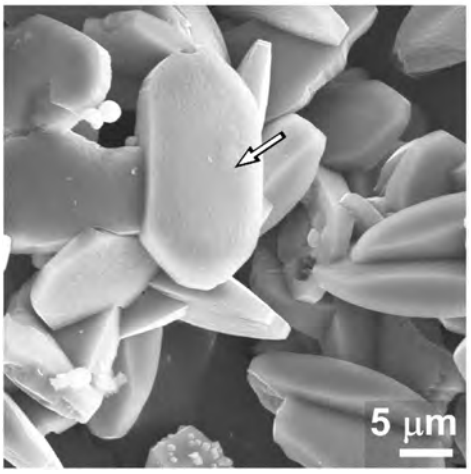

Figure 6. Scanning electron micrograph of a conventional mordenite prepared by an organic-free synthesis using Na^{+} as an inorganic structure-directing agent. The arrow highlights a six-edged surface that is characteristic of many **MOR**-type crystals reported in the literature. This surface is commonly indexed as the (001) face.

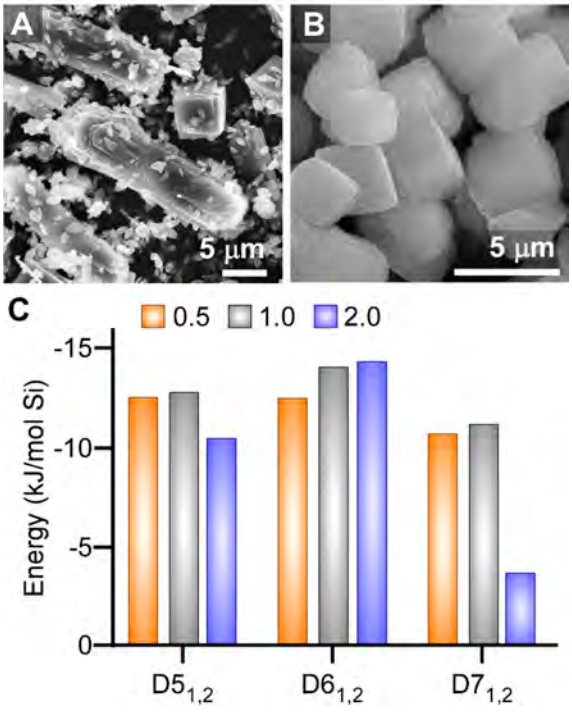

Figure 7. Scanning electron micrographs of the HOU-4 synthesis using a combination of TMAda^{+} with (A) 1,2-pentanediol and (B) 1,2-propanediol. Crystals in (A) contain mixed phases of mordenite and SSZ-13 (isometric crystals), while those in (B) are pure SSZ-13 by XPD. (C) Stabilization energy from MD calculations as a function of x alcohols per unit cell (x = 0.5, 1.0, 2.0) for a fixed loading of 1.5 TMAda^{+} per unit cell. We find that D6$_{1,2}$ at a loading of 1.0−2.0 molecules per unit cell provides the greatest stabilization.

carbon lengths in excess of six were not tested owing to their immiscibility in water. The results of diol substitution are consistent with MD simulations of mordenite with TMAda^{+} and diols of varying carbon length. At a fixed TMAda^{+} content and varying diol quantities, the minimum in the stabilization energy (Figure 7C) for D6$_{1,2}$ indicates that the combination of this diol with TMAda^{+} is an energetically favorable pairing for

DOI: 10.1021/jacs.9b09697
J. Am. Chem. Soc. 2019, 141, 20155−20165

HOU-4 synthesis, consistent with experimental observations. Thus, both experiment and simulation suggest that $D6_{1,2}$ is optimal in size to span the 8-ring pockets and direct their growth.

It is not fully understood how the platelike morphology of HOU-4 crystals is derived from the combined structure-directing influences of $TMAda^+$ and $D6_{1,2}$ molecules. The dual action of organics enhances growth along the direction of channels (*c* direction) while hindering growth in the *a* direction. The role of cooperative OSDAs in HOU-4 crystallization is seemingly unrelated to that of a growth modifier which alters the crystal morphology in conventional mordenite synthesis, as neither organic solely produces thin crystals. In fact, the presence of $D6_{1,2}$ has the opposite effect in conventional mordenite syntheses, where it increases crystal thickness in the absence of $TMAda^+$ (Figure S26) relative to the control (Figure 6). The ability to prepare nanosized crystals has significant implications for catalytic applications. Zeolite catalysts with restricted mass transport, such as mordenite and other one-dimensional framework types, are the most susceptible to rapid deactivation by coking. Comparisons between HOU-4 and conventional mordenite crystals reveal that the crystal dimensions along the *c* direction (parallel to the large-pore channels) are comparable, on the order of a micrometer; however, the generation of ultrathin platelets leads to higher specific surface area, which can influence catalytic performance. To illustrate this point, we prepared acid forms of the platelets (H-HOU-4) and conventional crystals (H-mordenite). For catalytic testing we selected a reaction where shape selectivity was not critical in order to assess differences in catalyst activity. To this end, we used cumene cracking as a model reaction to evaluate time-on-stream lifetime. The total number of acid sites on each sample was quantified by NH_3 temperature-programmed desorption (TPD). Tests in a packed-bed reactor at 450 °C reveal that the turnover number (evaluated in the shaded regions of Figure 8) is much larger for H-HOU-4 (38.7 mol cumene/mol H^+) in comparison to conventional mordenite (10.3 mol cumene/mol H^+) owing to the faster rate of H-mordenite deactivation. These results are qualitatively consistent with studies of nanosized zeolite catalysts in the literature[2,45] that generally report much longer lifetimes owing to reduced mass transport limitations. For the study reported here, external acid sites probably play a role in the observed differences; however, it remains to be determined if the lack of stacking faults in HOU-4 improves internal mass transport and contributes to its improved lifetime. The different synthesis conditions may also yield distinct distributions of framework Al heteroatoms and associated Brønsted acid sites in H-mordenite and H-HOU-4, which would influence the catalytic activity and stability. Rationalizing the differences in catalyst performance is a topic of ongoing investigation.

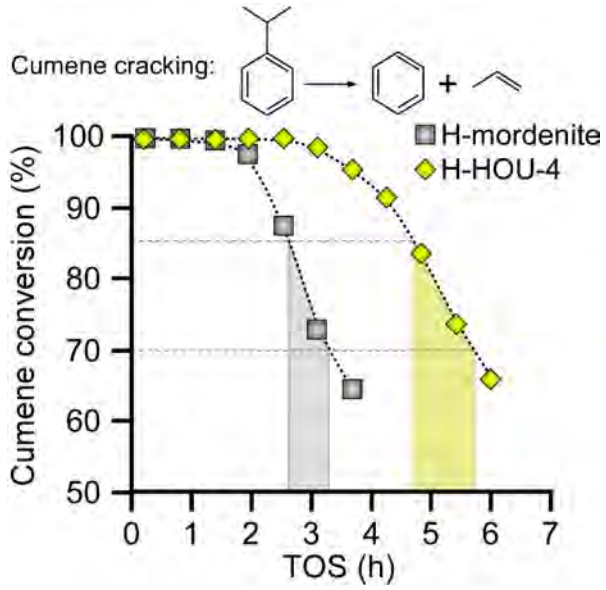

Figure 8. Comparative catalytic performance of H-mordenite crystals (Si/Al = 8 by EDX) from a conventional synthesis and H-HOU-4 crystals (Si/Al = 9.5 by EDX). Cumene cracking was performed in a packed-bed reactor at 450 °C using a weight hourly space velocity (WHSV) of 2 h^{-1}. The shaded regions were used to calculate catalyst turnover number using the density of acid sites as determined by NH_3-TPD to account for the different number of active (Brønsted acid) sites for each catalyst.

CONCLUSION

The generation of HOU-4 crystallites using a combination of two organics is one of only a few reported cases where multiple OSDAs work cooperatively to direct zeolite crystallization and structure. Using a collection of high-resolution characterization and modeling techniques, we are able to resolve the locations of both OSDAs in the pores of HOU-4. Combined synchrotron XPD, 2D solid-state NMR, HRTEM, and molecular modeling analyses reveal the framework structure and local compositions, types of framework–organic interactions, and relative distributions of organics within the 12-ring channels and 8-ring pockets of mordenite. The combination of these complementary techniques offers unparalleled insight into the roles of different OSDAs in directing zeolite crystallization to achieve distinct properties. We expect that the methods and analyses reported here can be extended to ascertain how SDAs tailor zeolite crystal size, shape, and composition. Indeed, one challenge in zeolite synthesis is determining how multiple organic and inorganic structure-directing species function in a concerted manner to influence the physicochemical properties of zeolites and control crystal polymorphism a priori. A unique aspect of HOU-4 crystallization is the role of nonionic alcohols, which interact relatively weakly with crystallizing zeolite frameworks and are rarely employed as OSDAs in zeolite syntheses. Here, diol molecules work in tandem with cationic Na^+ and $TMAda^+$ species to stabilize the different linear nanopore networks in mordenite.

The synthesis of nonfaulted submicrometer mordenite crystals has been a significant challenge. In this study, we have shown that the ability to prepare mordenite crystals with reduced stacking faults and high surface area improves the catalyst lifetime 4-fold relative to materials prepared by conventional methods. Collectively, our findings suggest that further exploration into the use of cooperative organics in zeolite syntheses holds considerable promise for the engineering and optimization of microporous materials.

EXPERIMENTAL SECTION

Materials. The following chemicals were used as reagents: Cab-O-Sil (M-5, Spectrum Chemical), silica gel (91%, Sigma-Aldrich), sodium hydroxide (98% pellets, MACRON Fine Chemicals), *N,N,N*-trimethyl-1,1-adamantammonium hydroxide (TMAda-OH, 25 wt % in water, SACHEM Inc.), 1,2-hexanediol ($D6_{1,2}$, 98%), 1,2-

DOI: 10.1021/jacs.9b09697
J. Am. Chem. Soc. 2019, 141, 20155–20165

pentanediol ($D5_{1,2}$, 96% Aldrich), 1,2-butanediol ($D4_{1,2}$, ≥98%, Sigma-Aldrich), 1,2-propanediol ($D3_{1,2}$, ≥99.5%, Sigma-Aldrich), and aluminum hydroxide (80.3 wt % $Al(OH)_3$, SPI0250 hydrogel). It should be noted that the IUPAC names for the two OSDAs used in this study are hexane-1,2-diol and 1-adamantyl(trimethyl)azanium. Ion exchange was performed using ammonium nitrate (ACS reagent ≥98%, Sigma-Aldrich). Deionized (DI) water used in all experiments was purified with an Aqua Solutions RODI-C-12A purification system (18.2 MΩ). All reagents were used as received without further purification.

Synthesis of Mordenite. Mordenite (HOU-4) was synthesized with the OSDA *N,N,N*-trimethyl-1,1-adamantammonium hydroxide (TMAda-OH) and 1,2-hexanediol ($D6_{1,2}$) using solutions with a molar composition of 0.052 $Al(OH)_3$/1.0 SiO_2/0.2 NaOH/44 H_2O/0.1 TMAda-OH/1.6 1,2-hexanediol. Sodium hydroxide (0.09 g, 0.0022 mol) was first dissolved in water (8.21 g, 0.4959 mol), followed by the addition of TMAda-OH (0.95 g, 0.0011 mol) and 1,2-hexanediol (2.17 g, 0.018 mol). This solution was stirred until it was clear (ca. 15 min). Aluminum hydroxide (0.06 g, 0.0005 mol) was added to the solution, and this mixture was stirred for another 15 min at room temperature. To this clear solution was added the silica source (0.67 g, 0.0112 mol), and the resulting mixture was first manually stirred with a plastic rod for ca. 15 min, followed by continuous stirring using a stir bar (400 rpm) for 4 h at 80 °C in a mineral oil bath. Approximately 10 g of growth solution after 4 h of heated stirring was placed in a Teflon-lined stainless steel acid digestion bomb (Parr Instruments) and was heated under rotation (~30 rpm) and autogenous pressure in a Thermo-Fisher Precision Premium 3050 Series gravity oven. The nominal time and temperature for HOU-4 synthesis was 6 days at 180 °C. The products of all syntheses were isolated as a white powder (ca. 600 mg) by centrifuging the mother liquor (13000 rpm for 45 min) for three cycles with DI water washes. Samples for microscopy were prepared by first redispersing a small amount of powder (ca. 5 mg) in DI water. An aliquot of this solution was placed on a glass slide and dried overnight. Crystals were transferred to metal sample disks for microscopy studies by contacting the glass slide with carbon tape for SEM.

Conventional mordenite was synthesized using a growth solution with a molar composition of 1 Al_2O_3/30 SiO_2/5 Na_2O/780 H_2O.[26,46] Sodium hydroxide (0.25 g, 0.0061 mol) was first dissolved in water (8.437 g, 0.468 mol), followed by the addition of sodium aluminate (0.1003 g, 0.00061 mol). The solution was stirred until it was clear (ca. 15 min), followed by the addition of silica gel (1.212 g, 0.0183 mol), and the resulting mixture was stirred at 400 rpm for 4 h. Approximately 10 g of the growth mixture was placed in a Teflon-lined stainless steel acid digestion bomb and was heated under static and autogenous pressure. The nominal time and temperature for synthesis was 4 days and 170 °C, respectively. The products of all syntheses were isolated from mother liquor using vacuum filtration and a 0.45 μm membrane filter with copious amounts of DI water washes. Samples for microscopy were prepared as described above.

Solid-State Nuclear Magnetic Resonance (NMR). Solid-state 1D and 2D ^1H, ^{13}C, ^{27}Al, and ^{29}Si MAS NMR spectroscopy was used to analyze the ^1H, ^{13}C, ^{27}Al, and ^{29}Si environments in as-made HOU-4 crystallites. The 2D $^{27}Al\{^{29}Si\}$ *J*-mediated NMR correlation spectrum (Figure 3A) was acquired on a Bruker ASCEND 400 MHz (9.4 T) DNP NMR spectrometer operating at Larmor frequencies of 400.203, 104.283, and 79.501 MHz for ^1H, ^{27}Al, and ^{29}Si nuclei, respectively. This instrument is equipped with a 3.2 mm triple-resonance HXY low-temperature MAS probehead. Low-temperature measurement conditions of 95 K were used for improved signal sensitivity. The spectrum was acquired using a 2D heteronuclear multiple quantum correlation (HMQC) pulse sequence[47,48] with an experimentally optimized half-echo τ delay of 20 ms used to refocus the weak (ca. $1/(4\tau)$ = 12.5 Hz) through-bond $^{27}Al-O-^{29}Si$ *J* couplings. The signal sensitivity was enhanced by applying a 1 ms ^{27}Al adiabatic double-frequency sweep pulse during the preparation period to invert the ^{27}Al satellite transitions.[49] During the rotor-synchronized τ delay periods, 100 kHz of continuous wave ^1H decoupling was applied. A recycle delay time of 1 s was used with a rotor-synchronized t_1 increment step size of 100 μs, 96 t_1 increments, and 256 transients for a total acquisition time of 7 h. The 2D $^{29}Si\{^1H\}$ and $^{13}C\{^1H\}$ spectra were acquired on a Bruker AVANCE 500 MHz (11.7 T) wide-bore spectrometer operating at Larmor frequencies of 500.222, 125.789, and 99.369 MHz for ^1H, ^{13}C, and ^{29}Si, respectively. Recycle delay times of 0.75 s were used with t_1 increment step sizes of 128 μs. The 2D $^{29}Si\{^1H\}$ HETCOR spectrum acquired at a short contact time (0.5 ms, Figure 3B) was acquired with 196 t_1 increments and 256 transients for a total acquisition time of 10.5 h. The 2D $^{29}Si\{^1H\}$ HETCOR spectrum acquired at a longer contact time (5 ms, Figure S19) was acquired with 256 t_1 increments and 64 transients for a total acquisition time of 3.5 h. The 2D $^{13}C\{^1H\}$ HETCOR spectra acquired with contact times of 0.5 and 5 ms (Figure S10) were acquired respectively with 250 and 430 t_1 increments and 512 and 128 transients for total acquisition times of 27 and 11.5 h. The 2D $^{27}Al\{^1H\}$ (Figure 3C) and $^{23}Na\{^1H\}$ (Figure S20) HETCOR spectra were acquired on a Bruker AVANCE-III Ultrashield Plus 800 MHz (18.8 T) narrow-bore spectrometer operating at Larmor frequencies of 208.527, 211.681, and 800.242 MHz for ^{27}Al, ^{23}Na, and ^1H, respectively, and a Bruker 3.2 mm broad-band double-resonance HX probehead was used. The 2D $^{27}Al\{^1H\}$ HETCOR spectrum was acquired with a repetition time of 1 s, 50 t_1 increments, and 512 transients for a total acquisition time of 7 h. The 2D $^{23}Na\{^1H\}$ HETCOR spectrum was acquired with a repetition time of 1 s, 32 t_1 increments, and 1024 transients for a total acquisition time of 9 h. All of the 2D HETCOR spectra were acquired using homonuclear $^1H-^1H$ eDUMBO-1_{22} decoupling[50] during the ^1H evolution periods to improve resolution in the ^1H dimensions. For the 2D $^{29}Si\{^1H\}$, $^{13}C\{^1H\}$, $^{23}Na\{^1H\}$, and $^{27}Al\{^1H\}$ HETCOR experiments, a variable-temperature chiller unit was to lower the sample temperature to approximately 263 K to reduce the mobility of the OSDA species and improve cross-polarization signal sensitivity. All of the 1D and 2D spectra were acquired with 100 kHz heteronuclear SPINAL-64[51] ^1H decoupling during the acquisition period.

Atomic Force Microscopy (AFM). AFM measurements were performed in air using an Asylum Research MFP-3D-SA instrument (Santa Barbara, CA). An aliquot of HOU-4 dispersed in water was placed on a silicon wafer and was allowed to dry at room temperature. The silicon wafer was calcined at 500 °C for 5 h, followed by cleaning under an inert Ar gas flow to remove loosely bound crystals. AFM images were collected using a Cr/Au-coated silicon nitride cantilever (Olympus RC800PB with a spring constant of 0.82 N/m) in contact mode at a scan rate of 1.2 Hz and 256 lines/scan.

Electron Microscopy. Scanning electron microscopy (SEM) was performed with a FEI 235 dual-beam (focused ion beam) system operated at 15 kV and a 5 mm working distance. All SEM samples were coated with a thin carbon layer (ca. 20 nm) prior to imaging. Transmission electron microscopy (TEM) was carried out for structural and morphology characterization using a Thermo Fischer (formerly FEI) 200 kV TitanX transmission electron microscope equipped with a windowless SDD Bruker EDS detector with fast processor.

X-ray Analysis. Energy-dispersive X-ray spectroscopy (EDX) was performed using a JEOL JSM 6330F field emission SEM at a working distance of 15 mm and voltage of 15 kV and 12 mA. X-ray powder diffraction (XPD) patterns of as-made zeolite samples were collected on a Siemens D5000 X-ray diffractometer using a Cu Kα_1 source (40 kV, 30 mA). For reference intensity ratio (RIR) analysis using mordenite−quartz mixtures, a Rigaku SmartLab diffractometer (40 kV, 44 mA) was used. The **MOR**-type framework was confirmed using a reference pattern from the Database of Zeolite Structures.[15] Synchrotron powder diffraction data were collected on an unwashed sample of HOU-4 in a 0.5 mm glass capillary on the Materials Science Beamline at the Swiss Light Source (SLS) in Villigen, Switzerland.[52] The wavelength was determined from a Si standard to be 0.7087 Å. Additional details of XPD analysis are provided in the Supporting Information.

DOI: 10.1021/jacs.9b09697
J. Am. Chem. Soc. 2019, 141, 20155−20165

Molecular Dynamics (MD) Simulations. MD simulations were performed with GROMACS 4.6.7.[53] The MOR zeolite framework was modeled as an all-silica structure using the ClayFF potential,[54] whereas the OSDAs (TMAda$^+$, 1,2-pentanediol, 1,2-butanediol, 1,2-hexanediol, and 1,2-heptanediol) were described using the generalized AMBER force field.[55] Atomic positions and lattice parameters for the mordenite framework were taken from the Database of Zeolite Structures. Na^+ ions were inserted into the 8-ring pockets, in the positions suggested by XRPD analysis (Figure S13). Although Na^+ ions stabilize Al in the framework, the positions of the Al sites are not precisely known. Consequently, Al was implicitly modeled by smearing a negative charge over the oxygens in the 8-ring pockets to counterbalance the Na^+ ions and ensure electroneutrality. Potential parameters for describing van der Waals interactions between the OSDAs and zeolite framework atoms were evaluated using standard Lorentz−Berthelot combining rules.[56] van der Waals and real-space Coulombic interactions were truncated using a cutoff of 0.9 nm, and the particle mesh Ewald method[56] was used to treat long-range electrostatics, with parameters chosen to ensure a relative error of less than 10^{-4} in the calculated energy. The equations of motion were propagated using a leapfrog integration scheme with a 2 fs time step.[56] The temperature and pressure of the system were maintained using a Bussi−Parrinello velocity-rescaling thermostat[57] and a Parrinello−Rahman barostat,[58] respectively. The relaxation time constants for both the thermostat and barostat were set to 2 ps.

Following our recent study of surfactant occlusion in MFI structured zeolites,[59] energetically favorable conformations for the OSDAs in mordenite were sampled using a three-step procedure. First, the OSDAs were gradually inserted into the zeolite framework using the alchemical transformation procedure described by Kim et al.,[60] whereby the OSDAs were converted from an ideal gas to fully interacting molecules over the course of a short MD simulation (500 ps) at ambient temperature. This gradual insertion step ensured that the system did not become trapped in unphysical, high-energy conformations. Next, the conjugate gradient algorithm was used to minimize the configurational energy of the system. Finally, the configuration from the energy minimization step was use to initialize a nanosecond-long MD simulation at 300 K and 0 bar. Data from the last half of the MD trajectory were to evaluate the stabilization energy[61,62] $E_s \equiv \langle U_{sys}\rangle - \langle U_{zeo}\rangle - \sum_i n_i \langle U_{SDA,i}\rangle$, where $\langle U_{sys}\rangle$ is the average energy of the system, $\langle U_{zeo}\rangle$ is the average energy of the empty zeolite framework, n_i is the number of inserted OSDA molecules of type i, and $\langle U_{SDA,i}\rangle$ is the average energy computed for a single OSDA molecule under vacuum. The steps above were repeated to evaluate E_s for $\sim 10^3$ different conformations at each OSDA loading considered in the study. Conformations with low E_s values (lowest 10%) were saved for subsequent analysis.

Catalyst Preparation and Testing. Samples for catalysis were calcined in a Thermo Fisher Lindberg Blue furnace under a constant flow of 100 sccm dried air (Matheson Tri-Gas) at 550 °C for 5 h with a temperature ramping/cooling rate of 1 °C/min. These samples were converted to an acid form (Brønsted acids) by ion exchange, wherein the calcined zeolite was mixed with 1.0 M ammonium nitrate solution to obtain a 2 wt % suspension. This mixture was heated to 80 °C for 2 h to allow the exchange of Na^+ with NH_4^+. This process was performed three times with centrifugation/washing between each ion exchange cycle. The final NH_4-−eolite samples were washed three times with DI water before they were calcined once again under the same conditions stated above, thus becoming H-form zeolite.

Cumene cracking over H-form catalysts was carried out in a 1/4 in. stainless steel tube installed in a Thermo Scientific Lindberg Blue M furnace. The catalyst bed was supported between two plugs of quartz wool, and a K-type thermocouple (Omega Engineering) was inserted into the stainless tube to measure the temperature of the catalyst bed. Prior to the reaction, the catalyst bed was pretreated in situ at 550 °C for 3 h under a flow of dried air (6 cm^3/min of O_2, 24 cm^3/min of N_2). After this pretreatment, the catalyst bed was cooled to the reaction temperature: i.e. 450 °C. Cumene (98%, Sigma-Aldrich) was fed by a syringe pump (Harvard Apparatus) at 2 μL/min into a heated inert gas stream of Ar (50 cm^3/min), which resulted in a reactant flow with a weight hourly space velocity (WHSV) of 2 h^{-1}. The cumene conversion is defined as the percentage of cumene reacted at the effluent of the catalyst bed. To compare the deactivation rate between different catalyst samples, the turnover number (TON) is calculated for a selected span of time-on-stream (TOS) using a modified form of the equation reported by Bhan and co-workers[63]

$$\mathrm{TON}(t) = \frac{1}{[\mathrm{H}^+]_0}\int_{t_1}^{t_2} F(\tau)\, \mathrm{d}\tau \tag{1}$$

where $[H^+]_0$ is the total number of Brønsted acid sites (obtained from the NH_3-TPD data in Table S3), $F(\tau)$ is the molar flow rate of converted carbon (reacted cumene), and t is the TOS selected between times t_1 and t_2 corresponding to 85 and 70% cumene conversion, respectively (i.e., regions of nearly linear deactivation in Figure 8).

Temperature-Programmed Desorption of Ammonia (NH_3-TPD). Temperature-programmed desorption of ammonia was performed by the Bhan group (University of Minnesota) on a Micromeritics Autochem II 2920 equipped with a TCD detector. Prior to TPD, ca. 100 mg of catalyst was first outgassed in He for 1 h at 600 °C with a heating ramp of 10 °C min^{-1}. Ammonia was adsorbed at 100 °C until saturatation, followed by flushing with He for 120 min at 100 °C. The ammonia desorption was monitored using a TCD detector until an upper temperature of 600 °C was reached with a ramp of 10 °C min^{-1}, using a flow of 25 mL min^{-1}.

■ ASSOCIATED CONTENT

Supporting Information

The Supporting Information is available free of charge at https://pubs.acs.org/doi/10.1021/jacs.9b09697.

Additional details of materials characterization, including XRD patterns, SEM and TEM images, TGA profiles, elemental analysis, solid-state NMR, AFM images and height profiles, details of molecular modeling, and examples of alternative synthesis conditions employing variants of OSDAs and the addition of modifiers (PDF)

Molecular dynamics simulations (MP4)

■ AUTHOR INFORMATION

Corresponding Authors

*E-mail for B.F.C.: bradc@engineering.ucsb.edu.

*E-mail for J.D.R.: jrimer@central.uh.edu.

ORCID

Zachariah J. Berkson: 0000-0002-2157-4172

Yufeng Shen: 0000-0001-9777-4691

Zhiyuan Zeng: 0000-0001-7483-1438

Haimei Zheng: 0000-0003-3813-4170

Jeremy C. Palmer: 0000-0003-0856-4743

Bradley F. Chmelka: 0000-0002-4450-6949

Jeffrey D. Rimer: 0000-0002-2296-3428

Author Contributions

All authors have given approval to the final version of the manuscript.

Notes

The authors declare no competing financial interest.

■ ACKNOWLEDGMENTS

J.D.R. acknowledges support primarily from the U.S. Department of Energy, Office of Science, Office of Basic Energy Sciences (Award DE-SC0014468). J.D.R. and J.C.P. acknowledge funding from the Welch Foundation (Award Nos. E-1794

DOI: 10.1021/jacs.9b09697
J. Am. Chem. Soc. 2019, 141, 20155−20165

and E-1882, respectively). Z.J.B. was supported by a grant from the BASF Corporation. The solid-state MAS NMR measurements at the University of California, Santa Barbara (UCSB), made use of the MRL Shared Experimental Facilities, which are supported by the MRSEC program of the NSF under Award No. DMR 1720256, a member of the Materials Research Facilities Network (www.mrfn.org). L.B.M. thanks Nicola Casati for his assistance with the synchrotron powder diffraction measurements on the Materials Science Beamline at the SLS in Villigen, Switzerland, and UCSB for hosting her as a visiting scholar. H.Z. acknowledges funding from DOE Office of Basic Energy Sciences, Materials Sciences and Engineering Division, under Contract No. DE-AC02-05-CH11231 within the KC22ZH program. We are grateful to M. F. Hsieh for help with catalyst testing and M. D. Susman for help with quartz calibration analysis. We thank A. Bhan and Z. Shi at the University of Minnesota for help with NH_3-TPD measurements.

REFERENCES

(1) Ng, E. P.; Chateigner, D.; Bein, T.; Valtchev, V.; Mintova, S. Capturing Ultrasmall EMT Zeolite from Template-Free Systems. *Science* **2012**, *335* (6064), 70−73.

(2) Zhang, X. Y.; Liu, D. X.; Xu, D. D.; Asahina, S.; Cychosz, K. A.; Agrawal, K. V.; Al Wahedi, Y.; Bhan, A.; Al Hashimi, S.; Terasaki, O.; Thommes, M.; Tsapatsis, M. Synthesis of Self-Pillared Zeolite Nanosheets by Repetitive Branching. *Science* **2012**, *336* (6089), 1684−1687.

(3) Olsbye, U.; Svelle, S.; Bjorgen, M.; Beato, P.; Janssens, T. V. W.; Joensen, F.; Bordiga, S.; Lillerud, K. P. Conversion of Methanol to Hydrocarbons: How Zeolite Cavity and Pore Size Controls Product Selectivity. *Angew. Chem., Int. Ed.* **2012**, *51* (24), 5810−5831.

(4) Rimer, J. D.; Kumar, M.; Li, R.; Lupulescu, A. I.; Oleksiak, M. D. Tailoring the physicochemical properties of zeolite catalysts. *Catal. Sci. Technol.* **2014**, *4* (11), 3762−3771.

(5) Bereciartua, P. J.; Cantin, A.; Corma, A.; Jorda, J. L.; Palomino, M.; Rey, F.; Valencia, S.; Corcoran, E. W.; Kortunov, P.; Ravikovitch, P. I.; Burton, A.; Yoon, C.; Wang, Y.; Paur, C.; Guzman, J.; Bishop, A. R.; Casty, G. L. Control of zeolite framework flexibility and pore topology for separation of ethane and ethylene. *Science* **2017**, *358* (6366), 1068−1071.

(6) Brand, S. K.; Schmidt, J. E.; Deem, M. W.; Daeyaert, F.; Ma, Y. H.; Terasaki, O.; Orazov, M.; Davis, M. E. Enantiomerically enriched, polycrystalline molecular sieves. *Proc. Natl. Acad. Sci. U. S. A.* **2017**, *114* (20), 5101−5106.

(7) Gallego, E. M.; Portilla, M. T.; Paris, C.; León-Escamilla, A.; Boronat, M.; Moliner, M.; Corma, A. Ab initio" synthesis of zeolites for preestablished catalytic reactions. *Science* **2017**, *355* (6329), 1051.

(8) Na, K.; Jo, C.; Kim, J.; Cho, K.; Jung, J.; Seo, Y.; Messinger, R. J.; Chmelka, B. F.; Ryoo, R. Directing Zeolite Structures into Hierarchically Nanoporous Architectures. *Science* **2011**, *333* (6040), 328−332.

(9) Simancas, R.; Dari, D.; Velamazan, N.; Navarro, M. T.; Cantin, A.; Jorda, J. L.; Sastre, G.; Corma, A.; Rey, F. Modular Organic Structure-Directing Agents for the Synthesis of Zeolites. *Science* **2010**, *330* (6008), 1219−1222.

(10) Jeon, M. Y.; Kim, D.; Kumar, P.; Lee, P. S.; Rangnekar, N.; Bai, P.; Shete, M.; Elyassi, B.; Lee, H. S.; Narasimharao, K.; Basahel, S. N.; Al-Thabaiti, S.; Xu, W. Q.; Cho, H. J.; Fetisov, E. O.; Thyagarajan, R.; DeJaco, R. F.; Fan, W.; Mkhoyan, K. A.; Siepmann, J. I.; Tsapatsis, M. Ultra-selective high-flux membranes from directly synthesized zeolite nanosheets. *Nature* **2017**, *543* (7647), 690−694.

(11) De Yoreo, J. J.; Gilbert, P.; Sommerdijk, N.; Penn, R. L.; Whitelam, S.; Joester, D.; Zhang, H. Z.; Rimer, J. D.; Navrotsky, A.; Banfield, J. F.; Wallace, A. F.; Michel, F. M.; Meldrum, F. C.; Colfen, H.; Dove, P. M. Crystallization by particle attachment in synthetic, biogenic, and geologic environments. *Science* **2015**, *349* (6247), aaa6760.

(12) Morris, S. A.; Bignami, G. P. M.; Tian, Y.; Navarro, M.; Firth, D. S.; Cejka, J.; Wheatley, P. S.; Dawson, D. M.; Slawinski, W. A.; Wragg, D. S.; Morris, R. E.; Ashbrook, S. E. In situ solid-state NMR and XRD studies of the ADOR process and the unusual structure of zeolite IPC-6. *Nat. Chem.* **2017**, *9* (10), 1012−1018.

(13) Olafson, K. N.; Li, R.; Alamani, B. G.; Rimer, J. D. Engineering Crystal Modifiers: Bridging Classical and Nonclassical Crystallization. *Chem. Mater.* **2016**, *28* (23), 8453−8465.

(14) Berkson, Z. J.; Messinger, R. J.; Na, K.; Seo, Y.; Ryoo, R.; Chmelka, B. F. Non-Topotactic Transformation of Silicate Nanolayers into Mesostructured MFI Zeolite Frameworks During Crystallization. *Angew. Chem., Int. Ed.* **2017**, *56* (19), 5164−5169.

(15) Baerlocher, C.; McCusker, L. B., Database of Zeolite Structures; http://www.iza-structure.org/databases/.

(16) Valtchev, V.; Tosheva, L. Porous Nanosized Particles: Preparation, Properties, and Applications. *Chem. Rev.* **2013**, *113* (8), 6734−6760.

(17) Chiang, H.; Bhan, A. Catalytic consequences of hydroxyl group location on the rate and mechanism of parallel dehydration reactions of ethanol over acidic zeolites. *J. Catal.* **2010**, *271* (2), 251−261.

(18) Grundner, S.; Markovits, M. A. C.; Li, G.; Tromp, M.; Pidko, E. A.; Hensen, E. J. M.; Jentys, A.; Sanchez-Sanchez, M.; Lercher, J. A. Single-site trinuclear copper oxygen clusters in mordenite for selective conversion of methane to methanol. *Nat. Commun.* **2015**, *6*, 7546.

(19) Rozanska, X.; van Santen, R. A.; Hutschka, F.; Hafner, J. A periodic DFT study of intramolecular isomerization reactions of toluene and xylenes catalyzed by acidic mordenite. *J. Am. Chem. Soc.* **2001**, *123* (31), 7655−7667.

(20) Gora-Marek, K.; Tarach, K.; Tekla, J.; Olejniczak, Z.; Kustrowski, P.; Liu, L. C.; Martinez-Triguero, J.; Rey, F. Hierarchical Mordenite Dedicated to the Fluid Catalytic Cracking Process: Catalytic Performance Regarding Textural and Acidic Properties. *J. Phys. Chem. C* **2014**, *118* (48), 28043−28054.

(21) Bhan, A.; Allian, A. D.; Sunley, G. J.; Law, D. J.; Iglesia, E. Specificity of sites within eight-membered ring zeolite channels for carbonylation of methyls to acetyls. *J. Am. Chem. Soc.* **2007**, *129* (16), 4919−4924.

(22) Boronat, M.; Martinez-Sanchez, C.; Law, D.; Corma, A. Enzyme-like Specificity in Zeolites: A Unique Site Position in Mordenite for Selective Carbonylation of Methanol and Dimethyl Ether with CO. *J. Am. Chem. Soc.* **2008**, *130* (48), 16316−16323.

(23) Vangeem, P. C.; Scholle, K.; Vandervelden, G. P. M.; Veeman, W. S. Study of the Transformation of Small-port into Large-port Mordenite by Magic Angle Spinning NMR and Infrared Spectroscopy. *J. Phys. Chem.* **1988**, *92* (6), 1585−1589.

(24) Simoncic, P.; Armbruster, T. Peculiarity and defect structure of the natural and synthetic zeolite mordenite: A single-crystal X-ray study. *Am. Mineral.* **2004**, *89* (2−3), 421−431.

(25) Pastvova, J.; Kaucky, D.; Moravkova, J.; Rathousky, J.; Sklenak, S.; Vorokhta, M.; Brabec, L.; Pilar, R.; Jakubec, I.; Tabor, E.; Klein, P.; Sazama, P. Effect of Enhanced Accessibility of Acid Sites in Micromesoporous Mordenite Zeolites on Hydroisomerization of n-Hexane. *ACS Catal.* **2017**, *7* (9), 5781−5795.

(26) Hincapie, B. O.; Garces, L. J.; Zhang, Q. H.; Sacco, A.; Suib, S. L. Synthesis of mordenite nanocrystals. *Microporous Mesoporous Mater.* **2004**, *67* (1), 19−26.

(27) Nosheen, S.; Galasso, F.; Suib, S. L. Synthesis of Mordenite Aggregates of Nanometer-Sized Crystallites. *Sci. Adv. Mater.* **2009**, *1* (1), 31−37.

(28) Ren, L. M.; Guo, Q.; Zhang, H. Y.; Zhu, L. F.; Yang, C. G.; Wang, L.; Meng, X. J.; Feng, Z. C.; Li, C.; Xiao, F. S. Organotemplate-free and one-pot fabrication of nano-rod assembled plate-like micro-sized mordenite crystals. *J. Mater. Chem.* **2012**, *22* (14), 6564−6567.

(29) Jo, C.; Jung, J.; Shin, H. S.; Kim, J.; Ryoo, R. Capping with Multivalent Surfactants for Zeolite Nanocrystal Synthesis. *Angew. Chem., Int. Ed.* **2013**, *52* (38), 10014−10017.

DOI: 10.1021/jacs.9b09697
J. Am. Chem. Soc. 2019, 141, 20155−20165

(30) Lobo, R. F.; Zones, S. I.; Davis, M. E. Structure-Direction in Zeolite Synthesis. *Journal of Inclusion Phenomena and Molecular Recognition in Chemistry* **1995**, *21* (1−4), 47−78.
(31) Corma, A.; Rey, F.; Rius, J.; Sabater, M. J.; Valencia, S. Supramolecular self-assembled molecules as organic directing agent for synthesis of zeolites. *Nature* **2004**, *431* (7006), 287−290.
(32) Xie, D.; McCusker, L. B.; Baerlocher, C.; Zones, S. I.; Wan, W.; Zou, X. D. SSZ-52, a Zeolite with an 18-Layer Aluminosilicate Framework Structure Related to That of the DeNOx Catalyst Cu-SSZ-13. *J. Am. Chem. Soc.* **2013**, *135* (28), 10519−10524.
(33) Zones, S. I.; Hwang, S. J. Synthesis of high silica zeolites using a mixed quaternary ammonium cation, amine approach: Discovery of zeolite SSZ-47. *Chem. Mater.* **2002**, *14* (1), 313−320.
(34) Camblor, M. A.; Corma, A.; Diaz-Cabanas, M. J.; Baerlocher, C. Synthesis and structural characterization of MWW type zeolite ITQ-1, the pure silica analog of MCM-22 and SSZ-25. *J. Phys. Chem. B* **1998**, *102* (1), 44−51.
(35) Turrina, A.; Garcia, R.; Watts, A. E.; Greer, H. F.; Bradley, J.; Zhou, W. Z.; Cox, P. A.; Shannon, M. D.; Mayoral, A.; Casci, J. L.; Wright, P. A. STA-20: An ABC-6 Zeotype Structure Prepared by Co-Templating and Solved via a Hypothetical Structure Database and STEM-ADF Imaging. *Chem. Mater.* **2017**, *29* (5), 2180−2190.
(36) Simoncic, P.; Armbruster, T.; Pattison, P. Cationic thionin blue in the channels of zeolite mordenite: A single-crystal X-ray study. *J. Phys. Chem. B* **2004**, *108* (45), 17352−17360.
(37) Zhang, L.; van Laak, A. N. C.; de Jongh, P. E.; de Jong, K. P. Synthesis of large mordenite crystals with different aspect ratios. *Microporous Mesoporous Mater.* **2009**, *126* (1−2), 115−124.
(38) Wu, Q. M.; Zhu, L. F.; Chu, Y. Y.; Liu, X. L.; Zhang, C. S.; Zhang, J.; Xu, H.; Xu, J.; Deng, F.; Feng, Z. C.; Meng, X. J.; Xiao, F. S. Sustainable Synthesis of Pure Silica Zeolites from a Combined Strategy of Zeolite Seeding and Alcohol Filling. *Angew. Chem., Int. Ed.* **2019**, *58* (35), 12138−12142.
(39) Berkson, Z. J.; Hsieh, M. F.; Smeets, S.; Gajan, D.; Lund, A.; Lesage, A.; Xie, D.; Zones, S. I.; McCusker, L. B.; Baerlocher, C.; Chmelka, B. F. Preferential siting of aluminum heteroatoms in the zeolite catalyst Al-SSZ-70. *Angew. Chem., Int. Ed.* **2019**, *58*, 6255−6259.
(40) Smeets, S.; Berkson, Z. J.; Xie, D.; Zones, S. I.; Wan, W.; Zou, X. D.; Hsieh, M. F.; Chmelka, B. F.; McCusker, L. B.; Baerlocher, C. Well-Defined Silanols in the Structure of the Calcined High-Silica Zeolite SSZ-70: New Understanding of a Successful Catalytic Material. *J. Am. Chem. Soc.* **2017**, *139* (46), 16803−16812.
(41) d'Espinose de la Caillerie, J. B.; Fretigny, C.; Massiot, D. MAS NMR spectra of quadrupolar nuclei in disordered solids: The Czjzek model. *J. Magn. Reson.* **2008**, *192* (2), 244−251.
(42) Anderson, M. W.; Barrie, P. J.; Klinowski, J. H-1 Magic-Angle-Spinning NMR-Studies of the Adsorption of Alcohols on Molecular-Sieve Catalysts. *J. Phys. Chem.* **1991**, *95* (1), 235−239.
(43) Qin, W.; Jain, R.; Hernandez, F. C. R.; Rimer, J. D. Organic-Free Interzeolite Transformation in the Absence of Common Building Units. *Chem. - Eur. J.* **2019**, *25* (23), 5893−5898.
(44) Kumar, M.; Luo, H.; Roman-Leshkov, Y.; Rimer, J. D. SSZ-13 Crystallization by Particle Attachment and Deterministic Pathways to Crystal Size Control. *J. Am. Chem. Soc.* **2015**, *137* (40), 13007−13017.
(45) Choi, M.; Na, K.; Kim, J.; Sakamoto, Y.; Terasaki, O.; Ryoo, R. Stable single-unit-cell nanosheets of zeolite MFI as active and long-lived catalysts. *Nature* **2009**, *461* (7261), 246−U120.
(46) Li, X. F.; Prins, R.; van Bokhoven, J. A. Synthesis and characterization of mesoporous mordenite. *J. Catal.* **2009**, *262* (2), 257−265.
(47) Garaga, M. N.; Hsieh, M. F.; Nour, Z.; Deschamps, M.; Massiot, D.; Chmelka, B. F.; Cadars, S. Local environments of boron heteroatoms in non-crystalline layered borosilicates. *Phys. Chem. Chem. Phys.* **2015**, *17* (33), 21664−21682.
(48) Lesage, A.; Sakellariou, D.; Steuernagel, S.; Emsley, L. Carbon-proton chemical shift correlation in solid-state NMR by through-bond multiple-quantum spectroscopy. *J. Am. Chem. Soc.* **1998**, *120* (50), 13194−13201.
(49) Van Veenendaal, E.; Meier, B. H.; Kentgens, A. P. M. Frequency stepped adiabatic passage excitation of half-integer quadrupolar spin systems. *Mol. Phys.* **1998**, *93* (2), 195−213.
(50) Elena, B.; de Paepe, G.; Emsley, L. Direct spectral optimization of proton-proton homonuclear dipolar decoupling in solid-state NMR. *Chem. Phys. Lett.* **2004**, *398* (4−6), 532−538.
(51) Fung, B. M.; Khitrin, A. K.; Ermolaev, K. An improved broadband decoupling sequence for liquid crystals and solids. *J. Magn. Reson.* **2000**, *142* (1), 97−101.
(52) Willmott, P. R.; Meister, D.; Leake, S. J.; Lange, M.; Bergamaschi, A.; Boge, M.; Calvi, M.; Cancellieri, C.; Casati, N.; Cervellino, A.; Chen, Q.; David, C.; Flechsig, U.; Gozzo, F.; Henrich, B.; Jaggi-Spielmann, S.; Jakob, B.; Kalichava, I.; Karvinen, P.; Krempasky, J.; Ludeke, A.; Luscher, R.; Maag, S.; Quitmann, C.; Reinle-Schmitt, M. L.; Schmidt, T.; Schmitt, B.; Streun, A.; Vartiainen, I.; Vitins, M.; Wang, X.; Wullschleger, R. The Materials Science beamline upgrade at the Swiss Light Source. *J. Synchrotron Radiat.* **2013**, *20*, 667−682.
(53) Hess, B.; Kutzner, C.; van der Spoel, D.; Lindahl, E. GROMACS 4: Algorithms for highly efficient, load-balanced, and scalable molecular simulation. *J. Chem. Theory Comput.* **2008**, *4* (3), 435−447.
(54) Cygan, R. T.; Liang, J. J.; Kalinichev, A. G. Molecular models of hydroxide, oxyhydroxide, and clay phases and the development of a general force field. *J. Phys. Chem. B* **2004**, *108* (4), 1255−1266.
(55) Wang, J. M.; Wolf, R. M.; Caldwell, J. W.; Kollman, P. A.; Case, D. A. Development and testing of a general amber force field (vol 25, pg 1157, 2004). *J. Comput. Chem.* **2005**, *26* (1), 114−114.
(56) Frenkel, D.; Smit, B. *Understanding molecular simulation: from algorithms to applications*, 2nd ed.; Academic Press: San Diego, CA, 2002.
(57) Bussi, G.; Donadio, D.; Parrinello, M. Canonical sampling through velocity rescaling. *J. Chem. Phys.* **2007**, *126* (1), 014101.
(58) Parrinello, M.; Rahman, A. Polymorphic Transitions in Single-Crystals - a New Molecular-Dynamics Method. *J. Appl. Phys.* **1981**, *52* (12), 7182−7190.
(59) Chawla, A.; Li, R.; Jain, R.; Clark, R. J.; Sutjianto, J. G.; Palmer, J. C.; Rimer, J. D. Cooperative effects of inorganic and organic structure-directing agents in ZSM-5 crystallization. *Mol. Syst. Des. Eng.* **2018**, *3* (1), 159−170.
(60) Kim, S. B.; Palmer, J. C.; Debenedetti, P. G. A Computational Study of the Effect of Matrix Structural Order on Water Sorption by Trp-Cage Miniproteins. *J. Phys. Chem. B* **2015**, *119* (5), 1847−1856.
(61) Davis, T. M.; Liu, A. T.; Lew, C. M.; Xie, D.; Benin, A. I.; Elomari, S.; Zones, S. I.; Deem, M. W. Computationally Guided Synthesis of SSZ-52: A Zeolite for Engine Exhaust Clean-up. *Chem. Mater.* **2016**, *28* (3), 708−711.
(62) Pophale, R.; Daeyaert, F.; Deem, M. W. Computational prediction of chemically synthesizable organic structure directing agents for zeolites. *J. Mater. Chem. A* **2013**, *1* (23), 6750−6760.
(63) Hwang, A.; Prieto-Centurion, D.; Bhan, A. Isotopic tracer studies of methanol-to-olefins conversion over HSAPO-34: The role of the olefins-based catalytic cycle. *J. Catal.* **2016**, *337*, 52−56.

DOI: 10.1021/jacs.9b09697
J. Am. Chem. Soc. 2019, 141, 20155−20165